# Clutter-Contaminated Signal Recovery in Spectral Domain for Polarimetric Weather Radar

Jiapeng Yin, Marc Schleiss, and Xuesong Wang

***Abstract*— The use of spectral polarimetric filters in the range-Doppler domain shows great promise for clutter mitigation in weather radar applications. One limitation of these filters is that they cannot deal with situations in which ground clutter and precipitation overlap. In this letter, we propose a new signal recovery technique based on kriging in the spectral domain to recover the precipitation in clutter-contaminated areas. Using synthetic radar data, we test our new method and compare its performance to that of Gaussian model adaptive processing and bilinear interpolation. Our results indicate that kriging is the most accurate and robust technique out of the three.**

***Index Terms*— Clutter-contaminated, ground clutter (GC), kriging, signal recovery, spectral-polarimetry, weather radar.**

## I. Introduction

POLARIMETRIC Doppler weather radar is a very effective remote sensing tool for gaining insights into the dynamics and microphysics of precipitation [1]. The prerequisite of using weather radar data is sufficient measurement accuracy, which needs to calibrate the radar system [2] and remove the clutter [3], [4]. Spectral polarimetric signal processing also appears to be very promising for clutter identification and mitigation. Two examples of this are the recently proposed double spectral linear depolarization ratio (MDsLDR) filter [3] and the object-orientated spectral polarimetric (OBSpol) filter [4]. Compared with the MDsLDR filter, the OBSpol filter has the advantage that it does not require cross-polar measurements (often not available), thus making it more broadly applicable.

The main limitation of spectral polarimetric filters such as MDsLDR and OBSpol is that they cannot deal well with cases in which clutter and precipitation overlap. When this occurs, the spectral polarimetric filters tend to keep the clutter-contaminated precipitation, resulting in biased estimates. Techniques such as the Clutter Environment ANalysis using Adaptive Processing (CLEAN-AP) [5] and Gaussian model adaptive processing (GMAP) [6] were proposed to solve this problem by trying to recover the precipitation signal that is embedded into ground clutter (GC). However, GMAP is based on the assumption that the spectral shapes of clutter and precipitation are Gaussian, which may not always be the case in practice [7]. Many versions of GMAP also assume that GC occupies a fixed spectral width over the whole range domain, which is not necessarily true for frequency modulation continuous wave radars where spectral leakage means GC tends to have larger spectral widths in the range bins near the radar [8].

To alleviate these problems, we propose an alternative and more flexible approach to signal recovery than GMAP. Our method starts by detecting and removing clutter-contaminated bins in the range-Doppler domain using the OBSpol filter and subsequently recovers the precipitation with the help of kriging [9] in areas where rainfall and GC overlap. The method is applied to synthetic clutter-contaminated precipitation measurements and performance is assessed by calculating the root mean square error and correlation coefficient of reflectivity, radial velocity, and spectrum width. Results show that signal recovery based on kriging is more stable and robust than GMAP, especially in cases where there is a lot of weak precipitation or overlap between precipitation and GC.

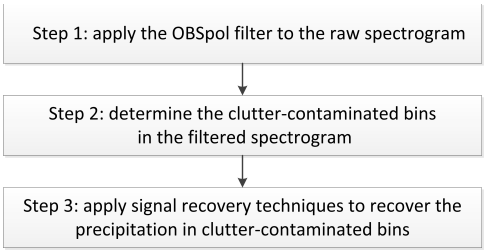


Fig. 1. Flowchart of the signal recovery techniques.

## II. Methodology

### A. General Approach

The clutter detection and removal technique is divided into three main steps as shown in Fig. 1. The input is the raw range-Doppler spectrogram and the output is the filtered spectrogram where the clutter has been removed and the precipitation recovered.

1) The OBSpol filter is applied to the raw range-Doppler spectrogram to generate a binary filtering mask for the clutter contaminated areas. Note that the OBSpol filter offers the option to apply a narrow notch filter around the central bins at 0 $ms^{-1}$ to mitigate GC. This notch filter is not really required here as GC will be identified in Step 2.

Manuscript received November 16, 2020; revised January 21, 2021 and February 22, 2021; accepted February 23, 2021. Date of publication March 12, 2021; date of current version December 20, 2021. This work was supported in part by the Postdoctoral International Exchange Program under Grant 48132 and in part by the Science and Technology Innovation Program of Hunan Province under Grant 2020RC2042. *(Corresponding author: Jiapeng Yin.)*

Jiapeng Yin and Xuesong Wang are with the College of Electronic Science and Technology, National University of Defense Technology, Changsha 410073, China (e-mail: jiapeng.yin@hotmail.com; wxs1018@vip.sina.com).

Marc Schleiss is with the Department of Geoscience and Remote Sensing, Delft University of Technology, 2628 CN Delft, Netherlands (e-mail: m.a.schleiss@tudelft.nl).

Digital Object Identifier 10.1109/LGRS.2021.3063355

2) In the case of GC, spectral polarimetric variable thresholding in combination with the central bin removal is applied to identify the clutter-contaminated precipitation bins remaining after the OBSpol filter. Normally, GC has larger power intensity, if the removal of GC is not sufficient, the residual clutter will strongly affect accuracy during signal reconstruction. The removal of the central bins around 0 $ms^{-1}$ guarantees that most of the GC with large intensity is removed. The spectral polarimetric variable thresholding is done by following the procedure in [10] and calculating the standard deviation $SDsZ_{dr}$ of the spectral differential reflectivity over a $3\times3$ sliding window in the range-Doppler spectrogram.
   Clutter-contaminated precipitation bins are identified iteratively for each range. For a given range $r$, if the filtering binary mask (obtained after Step 1) does not contain 0 $ms^{-1}$, the range is declared free of GC; otherwise clutter is identified by comparing the $SDsZ_{dr}(r, v)$ values to a fixed threshold of 2 dB (for more details about the effects of this threshold, the reader is referred to the sensitivity analysis). The clutter detection starts with the bin where $v$ corresponds to 0 $ms^{-1}$, moving toward larger velocities until $SDsZ_{dr}(r, v)$ is smaller than the prescribed threshold. All the clutter-contaminated bins in the spectrogram are regarded as areas "to-be-recovered."

**3)** Different signal recovery techniques are applied to the filtered spectrograms to estimate the values of the spectral reflectivity in the "to-be-recovered" bins. Specifically, three different techniques are used (bilinear interpolation, GMAP, and kriging).

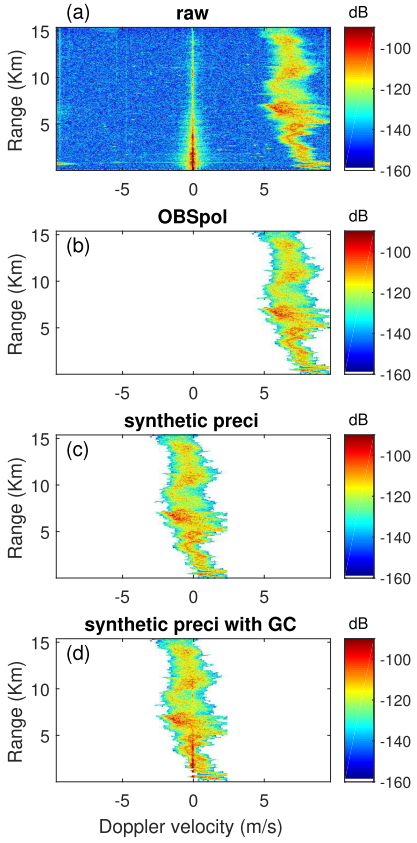


Fig. 2. Range-Doppler spectrogram of IDRA. (a) Raw. (b) OBSpol filtered. (c) Synthetic precipitation centered at 0 $ms^{-1}$. (d) Synthetic GC-contaminated precipitation centered 0 $ms^{-1}$.

### *B. Signal Recovery Techniques*

The different signal recovery techniques considered in this work are bilinear interpolation, kriging, and GMAP. The first two methods are implemented in the range-Doppler domain while GMAP is applied iteratively for each range.

*1) Bilinear Interpolation:* This is a simple non-parametric method that makes no assumption about the structure and distribution of the data. The version used in this letter is implemented in the function "interp.surface()" of the R package "fields" [11]. Its main purpose is to serve as a benchmark against which the performance of more advanced recovery techniques can be evaluated.

*2) Kriging:* The second method for recovering the clutter-contaminated precipitation signal is ordinary kriging applied on the spectral reflectivity and implemented using the R package "gstat" [12]. The sample variogram was estimated and fitted automatically using the "automap" [13] package. Since the covariance structure might be different along the range and Doppler dimensions, geometric anisotropy is used. The direction of principal variation and anisotropy ratio is determined with the help of the "intamap" [14] package. By default, anisotropy is ignored unless the estimated ratio between the major and minor axis is larger than 10%.

*3) GMAP:* The version of GMAP that is used in this letter is slightly different from the original one in [6] where windows are adapted depending on the signal to clutter ratio. The version of GMAP that we used has a fixed window (i.e., Hamming window) applied to the raw IQ data. The main problem with this approach is that in order for GMAP to estimate a Gaussian spectrum and recover the precipitation signal, a minimum number of clutter-free bins need to be available at each range. As a result, GMAP may not be applicable for all ranges. The default solution in this case is to ignore the problematic bins (i.e., do not recover the precipitation in them).

### *C. Performance Evaluation*

To assess the performance of the recovery techniques described above, measurements from a scanning Doppler polarimetric X-band radar named IDRA [3] are considered. IDRA rotates horizontally at the speed of 1 round/min at a fixed elevation angle of 0.5°. Its range and Doppler velocity resolutions are 30 m (512 samples) and 3.8 cm/s (512 samples), respectively.

The IDRA data are used to generate synthetic spectrograms in which GC overlaps with precipitation, as shown in Fig. 2. Fig. 2(a) shows the raw range-Doppler spectrogram at 13:00 UTC on August 22, 2014 which includes both precipitation and GC. Fig. 2(b) shows the spectrogram after applying the OBSpol filter. Since, in this case, GC does not overlap with precipitation, no further processing is necessary. Using this ideal case, we generate a synthetic spectrogram for

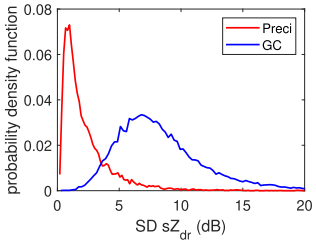


Fig. 3. Probability density functions for $SDsZ_{dr}$ of precipitation and GC.

testing the signal recovery algorithm for the case where GC and precipitation are overlapping. This is done by identifying, for each range, the Doppler bin with the maximum value in Fig. 2(b) and shifting it to 0 $\text{ms}^{-1}$ as shown in Fig. 2(c). The GC with Doppler velocity within $\pm$ 0.3 $\text{ms}^{-1}$ in Fig. 2(a) is then added to the shifted precipitation to create a synthetic GC-contaminated precipitation spectrogram as shown in Fig. 2(d). The latter is given as input to the signal recovery techniques. In total, 84 synthetic spectrograms (corresponding to a full PPI scan) were generated in this way.

The performance of the recovery algorithm is assessed by computing the root mean square error (RMSE) $\delta X$ and correlation coefficient (CC) $\rho X$ of the reflectivity $Z_{hh}$, mean Doppler velocity $\bar{v}$ and spectral width $\sigma_v$ for each of the 84 spectrograms assuming the truth is given by the shifted synthetic precipitation as shown in Fig. 2(c)

$$\delta X = \sqrt{\frac{1}{N}\sum_{n=1}^{N}\left(\hat{X}_{r_n} - X_{r_n}\right)^2} \tag{1}$$

and

$$\rho X = \frac{1}{N-1}\sum_{n=1}^{N}\left(\frac{\hat{X}_{r_n} - \mu_{\hat{X}}}{\sigma_{\hat{X}}}\right)\left(\frac{X_{r_n} - \mu_X}{\sigma_X}\right) \tag{2}$$

where $\hat{X}_{r_n}$ and $X_{r_n}$ are the estimated and true values of $X$ for the $n^{\text{th}}$ range bin; $\mu_{\hat{X}}$ and $\mu_X$ stand for their mean values and $\sigma_{\hat{X}}$ and $\sigma_X$ for their standard deviations. This is done for each variable $X$ of interest (i.e., $Z_{hh}$, $\bar{v}$ and $\sigma_v$). Note that for reflectivity, the metrics are calculated using the values in dB.

## III. Results

### A. Separation of Precipitation and Clutter

The first part focuses on the identification and separation of GC and precipitation in the range-Doppler domain based on $SDsZ_{dr}$ thresholding in combination with central bin removal.

The $SDsZ_{dr}$ is calculated over overlapping windows of size $3\times3$. Its probability density functions for GC and precipitation are displayed in Fig. 3. They were computed by combining five randomly selected spectrograms in which precipitation and GC were manually obtained. The peak value of the precipitation part is around 1 dB which is significantly smaller than that of the GC. The intersection point is around 3.5 dB which means that the optimal threshold for separation lies somewhere between 1 and 3.5 dB. Based on these results, we selected a threshold of 2 dB, corresponding to a false-positive rate of 0.5% and a false-negative rate of 37%. As is mentioned in Section II-A, any residual clutter will strongly affect accuracy during signal reconstruction, so it is better to remove too much than too little. For the GC removal, the central 4 bins are removed, in combination with 2-dB $SDsZ_{dr}$ thresholding. Note that the central 4 bins are the 4 bins in the spectrogram closest to 0 $\text{ms}^{-1}$ (for a fixed range), which are the most likely to contain GC with the largest intensity.

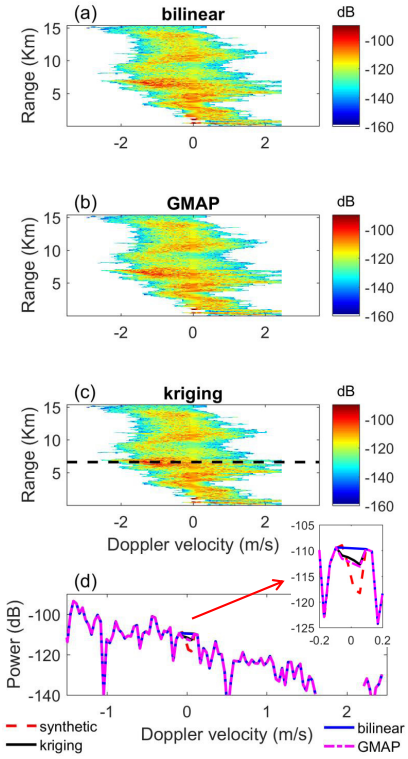


Fig. 4. Illustration of different signal recovery techniques. Range-Doppler spetrogram: (a) bilinear; (b) GMAP; (c) kriging; (d) Doppler spectrum of Range bin 220 [the dashed line in (c)].

More details about the sensitivity of the results to the selected thresholds are given in Section III-C.

### B. Signal Recovery

Using 2-dB $SDsZ_{dr}$ thresholding combined with central 4 bins removal, the "to-be-recovered" bins in the range-Doppler domain are determined and the remaining bins are used to interpolate the precipitation signal in the missing bins. Fig. 4 shows some examples of recovered spectrograms for the three different recovery techniques (bilinear, GMAP, and kriging). It shows that GMAP and kriging outperform bilinear interpolation with $\delta Z_{hh}$ of 1.90 dB (bilinear), 0.77 dB (GMAP) and 0.71 dB (kriging); and $\rho Z_{hh}$ of 0.90, 0.97 and 0.98. For comparison purposes, note that values of RMSE and correlation for the contaminated signal are 4.14 dB and 0.83, respectively. Similar results are obtained for the mean Doppler velocity $\bar{v}$ and spectral width $\sigma_v$.

To get more insights into the workings of the different recovery techniques, the Doppler spectrum of range 220 (i.e., 6.6 km from the radar) is displayed in Fig. 4(d). Since in this example, the spectrum is not Gaussian, GMAP does not perform well.

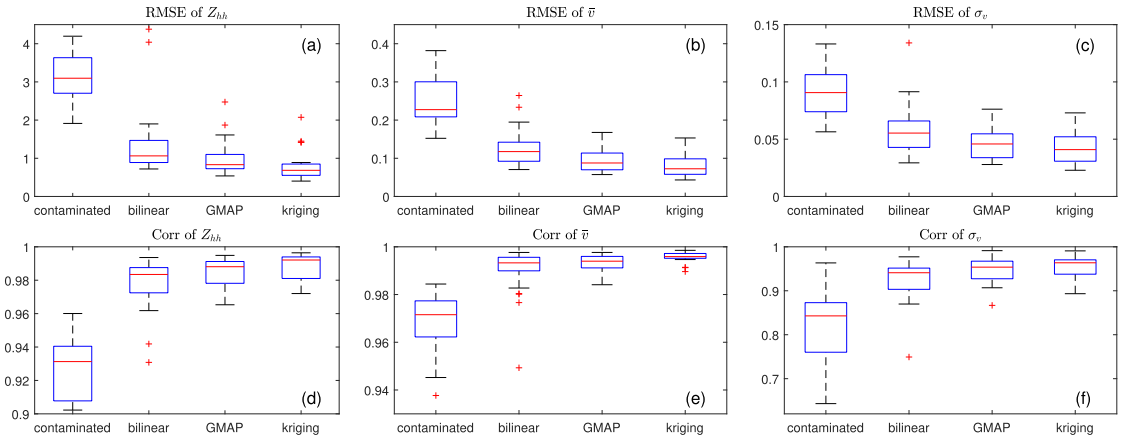


Fig. 5. RMSE and CC of different recovery techniques applied to reflectivity (a) and (d), mean Doppler velocity (b) and (e) and spectral width (c) and (f). (On each box, the central mark indicates the median, and the bottom and top edges of the box indicate the 25th and 75th percentiles, respectively. The whiskers extend to the most extreme data points not considered outliers, and the outliers are plotted individually using the "+" symbol.)

Next, we summarize the results obtained by applying the recovery techniques to the 84 spectrograms of the PPI. The threshold of $SDsZ_{dr}$ for GC identification was fixed to 2 dB, and the number of central bins to be removed was set to 4. Performance is summarized by boxplots of RMSE and correlation coefficients for $Z_{hh}$, $\bar{v}$ and $\sigma_v$ in Fig. 5. Since all boxplots look similar, only the ones for $Z_{hh}$ will be discussed. For comparison, note that the uncorrected, GC-contaminated reflectivity has a median error of more than 3 dB. By applying the signal recovery techniques, this bias can be reduced to about 1 dB. Among all considered techniques, kriging has the lowest RMSE (0.68 dB) and highest CC (0.99), followed by GMAP (RMSE 0.83 dB and CC 0.99) and bilinear interpolation (1.06 dB and CC 0.98). Note that GMAP has a smaller median error than bilinear interpolation but also a slightly larger spread.

To get more insights into the distribution of the errors, scatterplots of true versus recovered reflectivity values are shown in Fig. 6. They show that when $Z_{hh}$ is larger than 20 dBZ, the influence of GC is limited. Note that this is not general but specific to the IDRA case used in this work. As expected, the largest errors (in dB scale) occur for low reflectivity values. Bilinear interpolation tends to have more bias for larger values than kriging and GMAP.

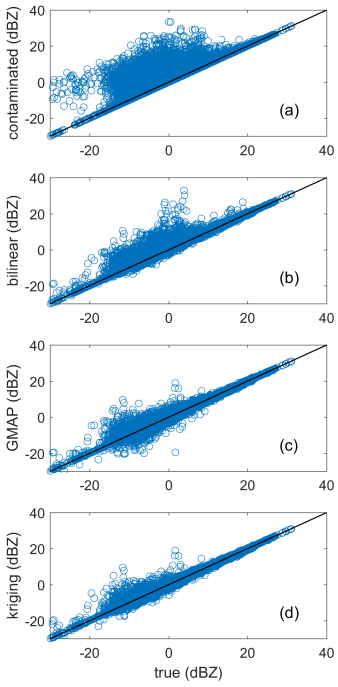


Fig. 6. Scatterplots of reflectivity values for different recovery methods: true reflectivity versus (a) contaminated values, (b) bilinear interpolation, (c) GMAP, and (d) kriging.

### C. Parameter Sensitivity Analysis

The sensitivity of the methods to the chosen model parameters is assessed according to a two-step procedure. First, the number of central bins removed during filtering is varied from 2 to 10 (with steps of 2). Then, for the optimal number of central bins, different $SDsZ_{dr}$ thresholds are explored for each method. To completely assess the recovery methods, precipitation without GC contamination is also considered. The data used are the same, namely 84 spectrograms of one PPI. As expected, Fig. 7(a) shows that when there is no GC contamination, the error increases as more central bins are removed. Conversely, for the case with GC, the error decreases with the number of bins removed. Overall, the removal of 6 central bins seems to lead to a good tradeoff.

Next, the number of central bins removed is set to 6 and the sensitivity to the choice of the $SDsZ_{dr}$ threshold is investigated using different values between 1 and 4 (in steps of 0.2). As can be seen in Fig. 5, the boxplots of $\delta Z_{hh}$ for the whole PPI are rather symmetric. Therefore, only the median values are reported. The results of GMAP and kriging are shown in Fig. 8(a).

As we move toward larger thresholds, the RMSE values first decrease, then increase and stabilize for larger thresholds. For kriging, the minimum is reached for a threshold of about 2 dB. When the $SDsZ_{dr}$ threshold is large, which means that the $SDsZ_{dr}$ thresholding has no effect on clutter removal, the performance of kriging and GMAP tend to be the same,

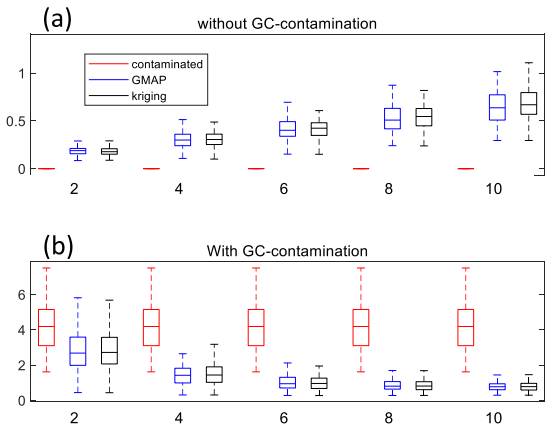


Fig. 7. RMSE of $Z_{hh}$ as a function of the number of central bins removed for cases (a) without GC-contamination and (b) with GC-contamination. Note that no $SDsZ_{dr}$ thresholding is applied.

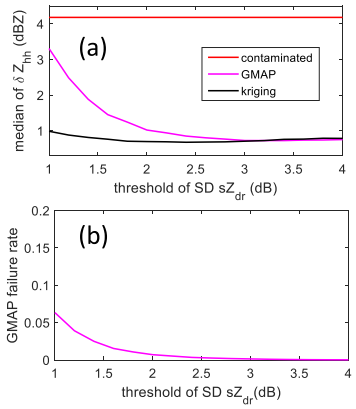


Fig. 8. Sensitivity analysis of different numbers of central bin removal on signal recovery performance. (a) Median of $\delta Z_{hh}$. (b) GMAP failure rate.

which is consistent with the results shown in Fig. 7(b). In addition, for thresholds below 1.6 dB, the performance of GMAP rapidly deteriorates. This is due to the high failure rate of GMAP as more and more precipitation gets labeled as clutter and not enough bins remain for the spectrum interpolation, as indicated in Fig. 8(b). By contrast, kriging considers the whole range-Doppler spectrogram for signal recovery, which is more robust.

Based on these facts, the optimal parameter selection for GC identification is 2 dB $SDsZ_{dr}$ thresholding in combination with central 6 bins removal. In this case, the RMSE of the kriging method applied to GC-contaminated $Z_{hh}$ data and cases without GC are 1 and 0.5 dB. Overall, the results indicate that signal recovery based on kriging is more stable and robust than GMAP.

## IV. Conclusion

Different spectral methods for recovering clutter-contaminated radar signals have been investigated, including bilinear interpolation, GMAP, and a new method based on kriging. The signal recovery methods can act as a follow-up process to spectral polarimetric filters, which integrate clutter identification and signal recovery. Synthetic radar data in which precipitation and GC overlap were generated to quantify the performance of these techniques and discuss their sensitivity to the choice of the underlying parameters. The results show that kriging provides the best estimates of reflectivity, radial velocity, and spectrum width, and is also the most robust technique.

One advantage of the kriging approach is that it can recover large areas without making too many assumptions about the shape of the clutter and precipitation in the spectral domain. This can be of advantage for other types of clutter as well, such as wind turbine clutter (WTC), for which GMAP would not perform well [6]. The key issue for WTC is to define good methods to reliably identify the clutter in the spectrogram, which is not trivial and requires more research. One promising possibility could be to use a threshold on the spectral width, which tends to be larger in clutter-contaminated areas due to the rotation of the blades. In addition, since clutter identification is related to signal recovery performance, more accurate, and robust clutter identification in the spectral domain is required.

## References

[1] Y. Wang, T.-Y. Yu, A. V. Ryzhkov, and M. R. Kumjian, "Application of spectral polarimetry to a hailstorm at low elevation angle," *J. Atmos. Ocean. Technol.*, vol. 36, no. 4, pp. 567–583, Apr. 2019.

[2] J. Yin, P. Hoogeboom, C. Unal, H. Russchenberg, F. van der Zwan, and E. Oudejans, "UAV-aided weather radar calibration," *IEEE Trans. Geosci. Remote Sens.*, vol. 57, no. 12, pp. 10362–10375, Dec. 2019.

[3] J. Yin, C. M. H. Unal, and H. W. J. Russchenberg, "Narrow-band clutter mitigation in spectral polarimetric weather radar," *IEEE Trans. Geosci. Remote Sens.*, vol. 55, no. 8, pp. 4655–4667, Aug. 2017.

[4] J. Yin, C. Unal, and H. Russchenberg, "Object-orientated filter design in spectral domain for polarimetric weather radar," *IEEE Trans. Geosci. Remote Sens.*, vol. 57, no. 5, pp. 2725–2740, May 2019.

[5] S. Torres, D. Warde, and D. Zrnic, "Signal design and processing techniques for WSR-88D ambiguity resolution: Part 15 the CLEAN-AP filter," Nat. Severe Storms Lab., Norman, OK, USA, Tech. Rep., 2012.

[6] A. Siggia and R. Passarelli, "Gaussian model adaptive processing (GMAP) for improved ground clutter cancellation and moment calculation," in *Proc. Eur. Radar Meteorol. Hydrol.*, vol. 2, 2004, pp. 421–424.

[7] T.-Y. Yu, R. R. Rondinel, and R. D. Palmer, "Investigation of non-Gaussian Doppler spectra observed by weather radar in a tornadic supercell," *J. Atmos. Ocean. Technol.*, vol. 26, no. 3, pp. 444–461, Mar. 2009.

[8] A. Melzer, A. Onic, F. Starzer, and M. Huemer, "Short-range leakage cancelation in FMCW radar transceivers using an artificial on-chip target," *IEEE J. Sel. Topics Signal Process.*, vol. 9, no. 8, pp. 1650–1660, Dec. 2015.

[9] C. Jean-Paul, *Geostatistics: Modeling Spatial Uncertainty*, 2nd ed. Hoboken, NJ, USA: Wiley, 2012.

[10] D. N. Moisseev and V. Chandrasekar, "Polarimetric spectral filter for adaptive clutter and noise suppression," *J. Atmos. Ocean. Technol.*, vol. 26, no. 2, pp. 215–228, Feb. 2009.

[11] D. Nychka, R. Furrer, J. Paige, and S. Sain, "Fields: Tools for spatial data," Univ. Corp. Atmos. Res., Boulder, CO, USA, Tech. Rep., 2017. [Online]. Available: https://www.image.ucar.edu/~nychka/Fields

[12] E. J. Pebesma, "Multivariable geostatistics in S: The gstat package," *Comput. Geosci.*, vol. 30, no. 7, pp. 683–691, Aug. 2004.

[13] P. H. Hiemstra, E. J. Pebesma, C. J. W. Twenhöfel, and G. B. M. Heuvelink, "Real-time automatic interpolation of ambient gamma dose rates from the dutch radioactivity monitoring network," *Comput. Geosci.*, vol. 35, no. 8, pp. 1711–1721, Aug. 2009.

[14] E. Pebesma *et al.*, "INTAMAP: The design and implementation of an interoperable automated interpolation Web service," *Comput. Geosci.*, vol. 37, no. 3, pp. 343–352, Mar. 2011.